Electronic Supplementary Material (ESI) for Physical Chemistry Chemical Physics.

Two-Photon Chemistry of Tetrahydrofuran in Clathrate Hydrates

Michael A. Michon, Pawel Chmielniak, Peter M. Weber and Christoph Rose-Petruck

Supplemental Information

SI.1 Pump Laser Characterization & Optical Setup

SI.1a Pump Spectrum & Power Calibration

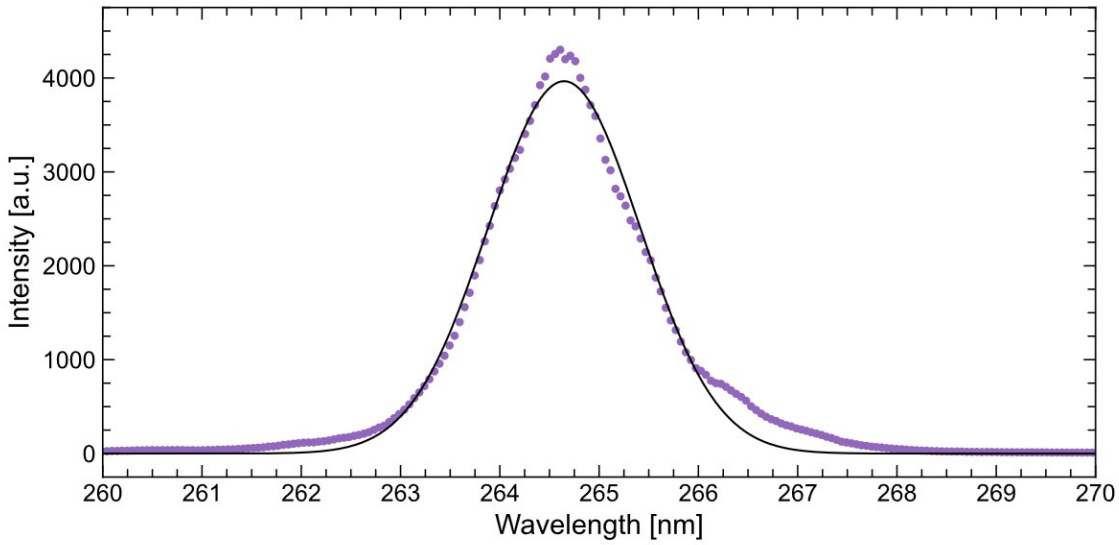

Figure S1: Ti:sapphire 3rd harmonic pump spectrum with Gaussian fit (solid line). Center frequency: 265 nm, FWHM: 1.8 nm.

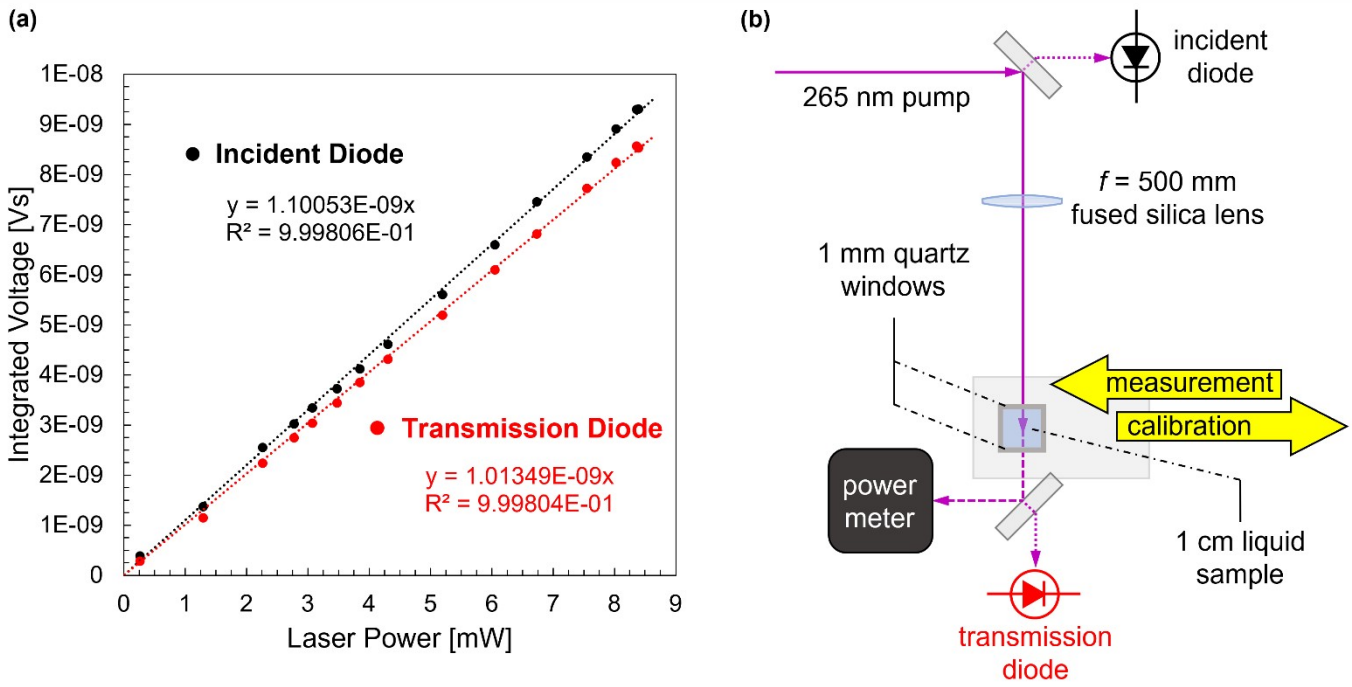

Figure S2: (a) Power calibration of GaP photodiodes (SM05PD7A) with 3 V reverse bias applied. Integrated voltage was taken as the area under the voltage vs. time response to a laser pulse output to an oscilloscope and power was measured using a power meter reading averaged over one minute. **(b)** Optical setup for transmittance measurements in liquid samples. The yellow arrows indicate the position of the sample either in or out of the beam path (purple arrows) for transmission measurement and calibration respectively. Diodes are placed to receive light leakage through mirrors (dotted arrows) before and after the sample so that incident and transmitted power can be measured simultaneously.

SI.1b Measurement of Temporal Pulse Profile

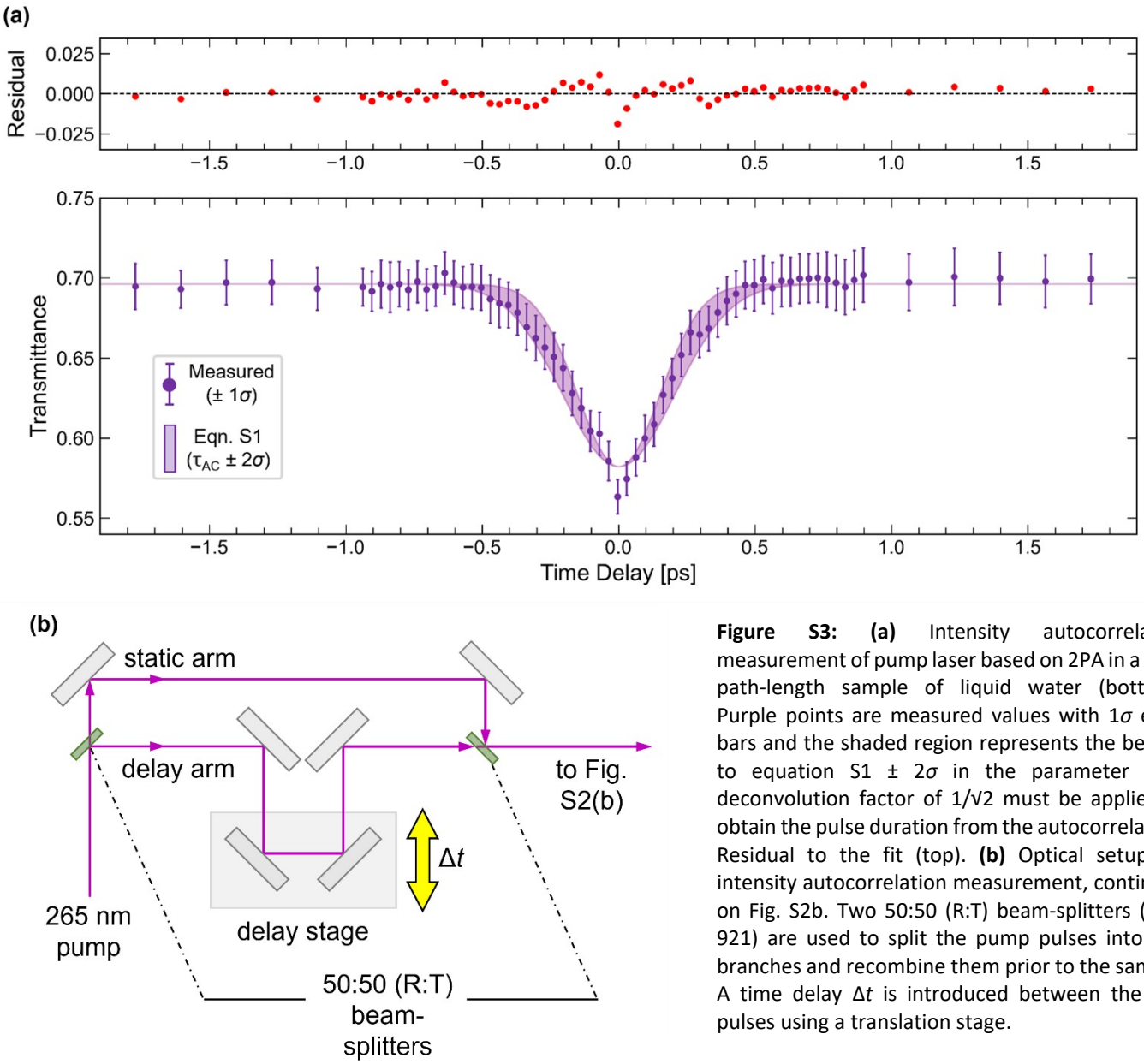

Figure S3: (a) Intensity autocorrelation measurement of pump laser based on 2PA in a 1 cm path-length sample of liquid water (bottom). Purple points are measured values with 1σ error bars and the shaded region represents the best fit to equation S1 ± 2σ in the parameter τ. A deconvolution factor of 1/√2 must be applied to obtain the pulse duration from the autocorrelation. Residual to the fit (top). **(b)** Optical setup for intensity autocorrelation measurement, continued on Fig. S2b. Two 50:50 (R:T) beam-splitters (#65-921) are used to split the pump pulses into two branches and recombine them prior to the sample. A time delay Δt is introduced between the two pulses using a translation stage.

$$T(t) = T_0 \exp\left(\frac{-t^2}{2\tau^2}\right) + T_\infty \qquad \textbf{Eqn. S1}$$

Table S1: Gaussian pulse width described by Eqn. S1. A deconvolution factor of 1/√2 must be applied to obtain τ_{pulse} from τ_{AC}:

		FWHM = $2\sqrt{(2\ln 2)}\tau$	1/e = $2\sqrt{(2)}\tau$	1/e^2 = 4τ
τ_{AC}	width of autocorrelation [fs]	419 ± 65	504 ± 78	712 ± 110
τ_{pulse}	width of pulse [fs]	296 ± 46	356 ± 55	504 ± 78

SI.1c Measurement of Spatial Beam Profile

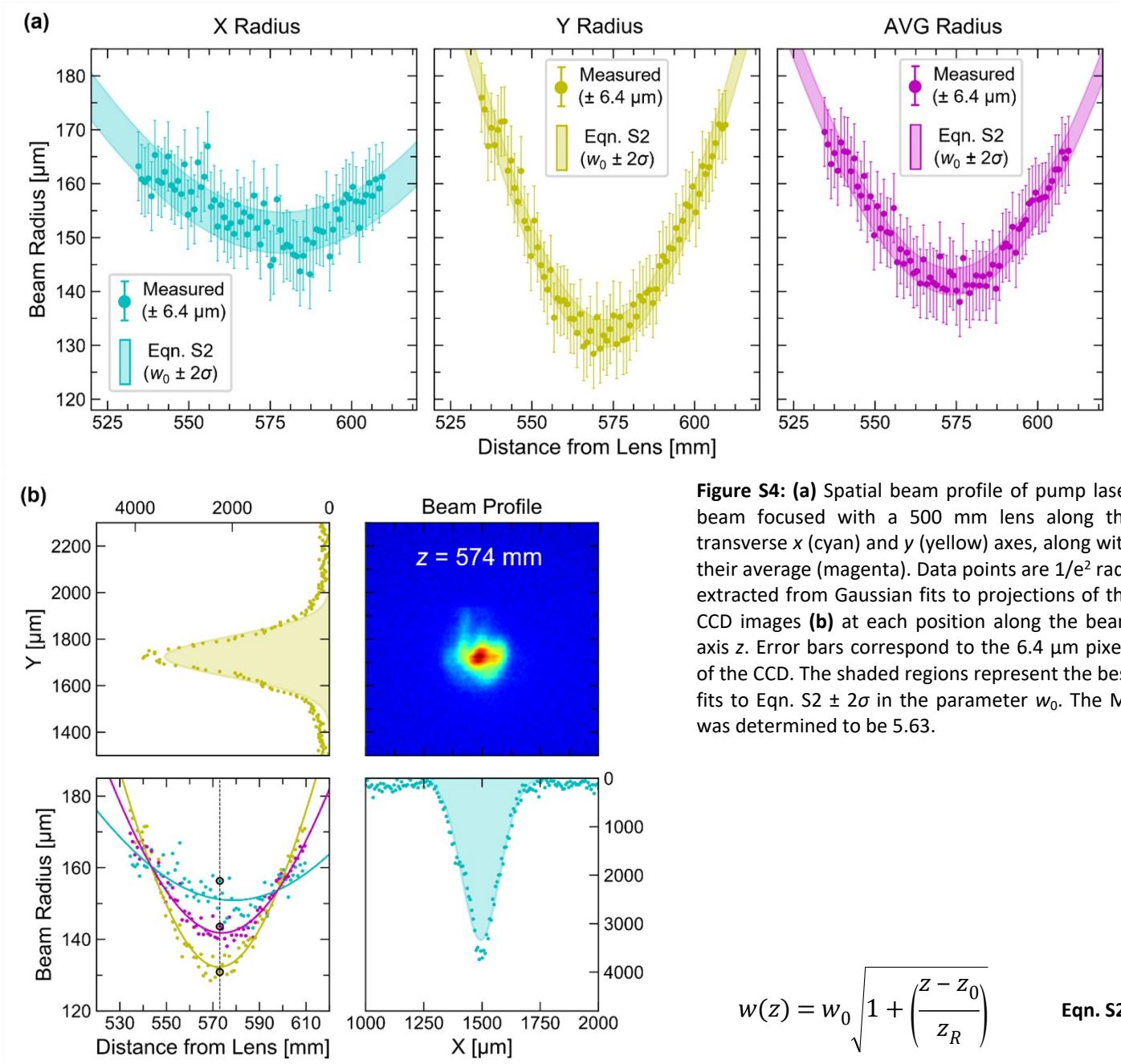

Figure S4: (a) Spatial beam profile of pump laser beam focused with a 500 mm lens along the transverse *x* (cyan) and *y* (yellow) axes, along with their average (magenta). Data points are $1/e^2$ radii extracted from Gaussian fits to projections of the CCD images **(b)** at each position along the beam axis *z*. Error bars correspond to the 6.4 µm pixels of the CCD. The shaded regions represent the best fits to Eqn. S2 ± 2σ in the parameter w_0. The M^2 was determined to be 5.63.

$$w(z) = w_0 \sqrt{1 + \left(\frac{z - z_0}{z_R}\right)^2} \qquad \textbf{Eqn. S2}$$

Table S2: Beam parameters extracted from a numerical fit to equation S2:

		X	Y	AVG
w_0	$1/e^2$ waist radius [µm]	151 ± 4	132 ± 3	142 ± 2
z_0	effective focal length [mm]	579 ± 35	573 ± 1	574 ± 2
z_R	Rayleigh range [mm]	98 ± 30	43 ± 3	57 ± 6

SI.1d Irradiation of Cryogenic Samples

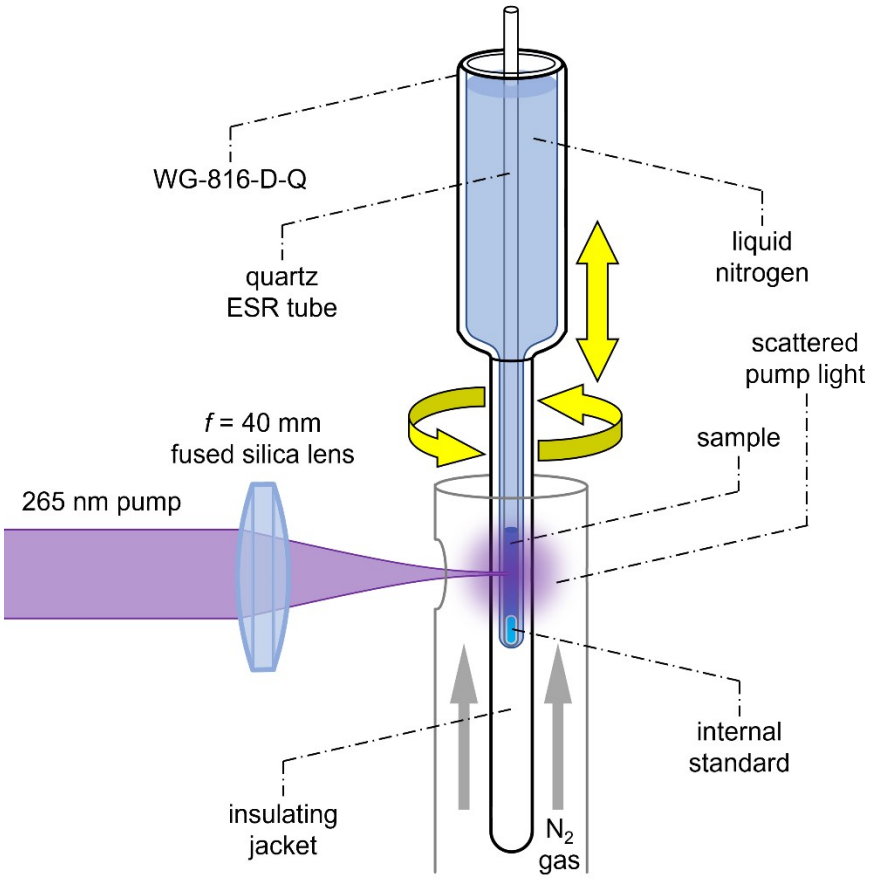

Figure S5: Experimental setup for the irradiation of cryogenic clathrate hydrates prior to ESR measurements. The liquid nitrogen cold-finger was cradled in a custom Teflon holder mounted to a piezo-controlled rotational stage, which itself was suspended from a vertically oriented linear actuator with 1 cm of travel. In this configuration, the bottom centimeter of the sample tube is positioned at beam height in the focus and continuously translated up and down one cycle per minute and rotated at ~0.5 rpm (yellow arrows) so that the laser is scanned along a helical path through the bottom centimeter of sample. The stem of the cold finger was sheathed in a 1-inch diameter tube and a gentle stream of nitrogen gas was continuously flowed through it to prevent moisture from condensing on the outer quartz, and a hole was drilled in the side at beam height to allow entry of the laser. The volume of liquid nitrogen in the cold finger was maintained during each 2-hour irradiation session by periodic refills at 15-minute intervals. The Cu(II)$SO_4 \cdot 5H_2O$ internal standard is located beneath the hydrate sample in the ESR tube.

SI.2 Sample Preparation & Characterization

SI.2a Clathrate Hydrate Crystal Growth

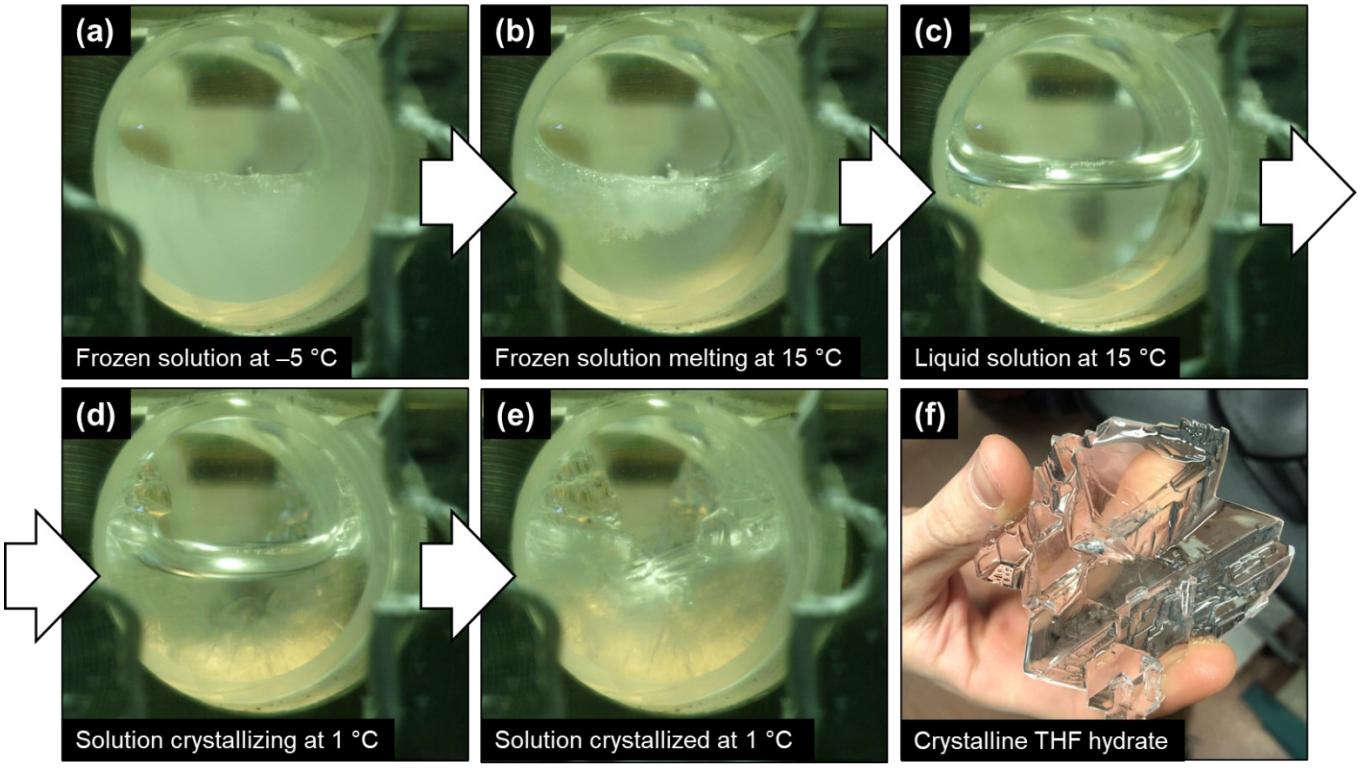

Figure S6: Qualitative evaluation of THF clathrate hydrates crystals grown from stoichiometric (5.88 mol%) aqueous THF solutions in a 1-inch diameter fused silica observation cell mounted on a thermoelectric cooler. Good thermal contact was established between the bottom and sides of the cell and a custom steel holder. The temperature was monitored with a thermocouple placed between the steel holder and the cell. **(a)** First, the temperature of the solution is held below the freezing point of water (0 °C) until freezing occurs. The result is completely opaque due to incomplete nucleation of the clathrate phase due to the formation of ice resulting in the exclusion of THF to interstitial spaces at grain boundaries. **(b-c)** Next, the solution is held at elevated temperature exceeding the melting points of both ice and the hydrate (~4.4 °C) until the solution has completely melted. **(d-e)** Lastly, the solution temperature is held above the freezing point of water, but below the nucleation temperature of the THF hydrate. The onset of crystal growth occurs rapidly thanks to the so-called "memory effect" established by the initial freezing cycle. **(f)** A large chunk of crystalline THF hydrate grown in a refrigerator using this general methodology. Crystals like this are crushed in liquid N_2 and used for ESR experiments.

SI.2b Raman Spectroscopy of Cryogenic Samples

Raman spectra were collected using a 532 nm laser at ~250 mW focused with the 40 mm fused silica lens. The Raman back-scatter was fiber coupled into an ARC SpectraPro-300i (300 mm focal length) monochromator through a 100 μm entrance slit and dispersed onto a Peltier-cooled SpectruMM-256HB (256×1024) CCD (pixel size ~25 μm) using either a 2400 or 1200 grooves/mm holographic diffraction grating. The spectral resolution of the gratings is estimated to be 2.25 cm^{-1} and 6.84 cm^{-1}, respectively. Spectra were baseline corrected using the asymmetric least squares method.[1]

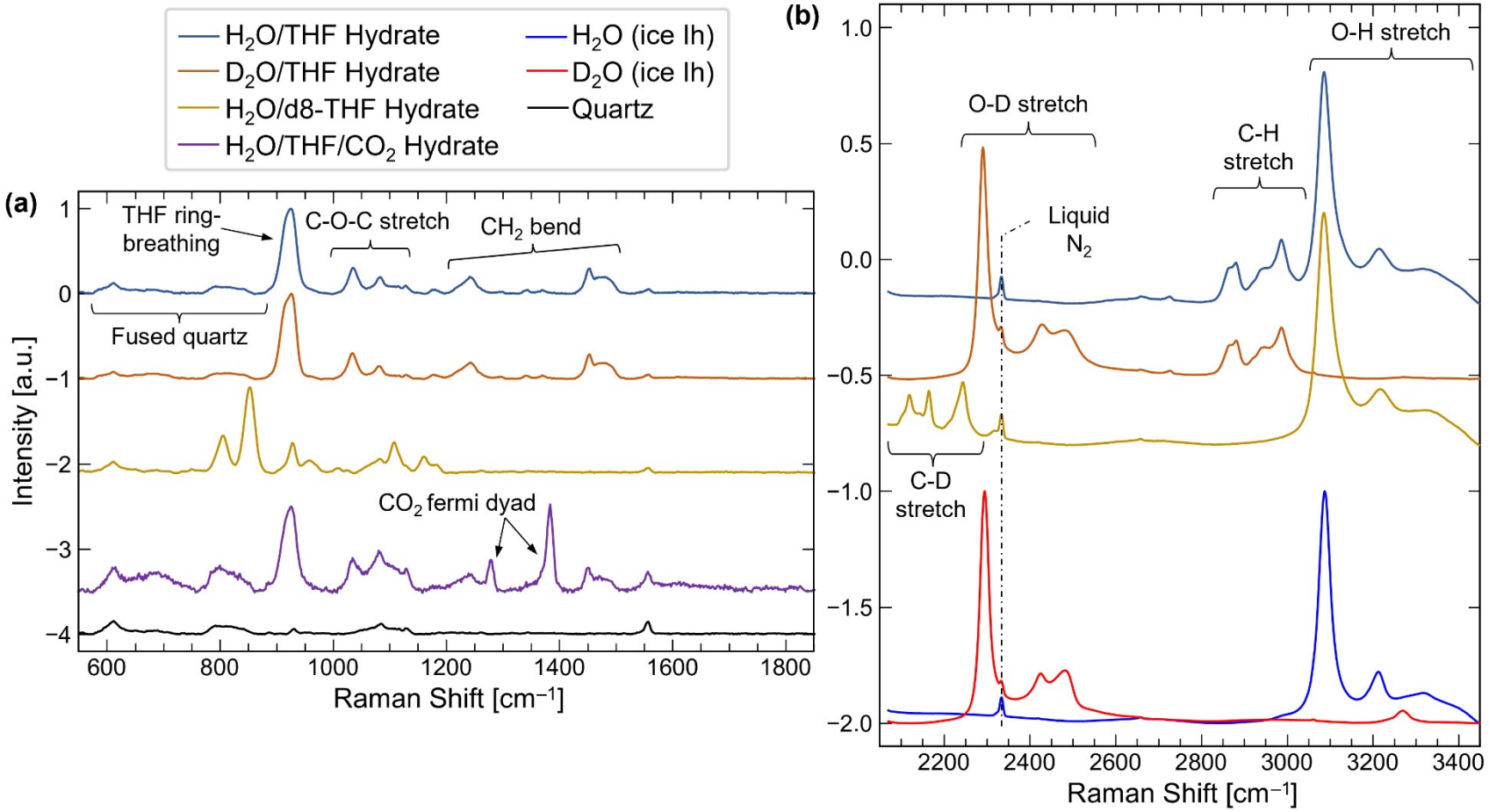

Figure S7: Raman spectra of cryogenic (77 K) THF hydrates in the low- **(a)** and high- **(b)** frequency regions. Comparison with liquid nitrogen quartz Dewar (black), H_2O (red) and D_2O (red) ice Ih. All samples exhibit the spectral characteristics expected of clathrate hydrates.[2–8]

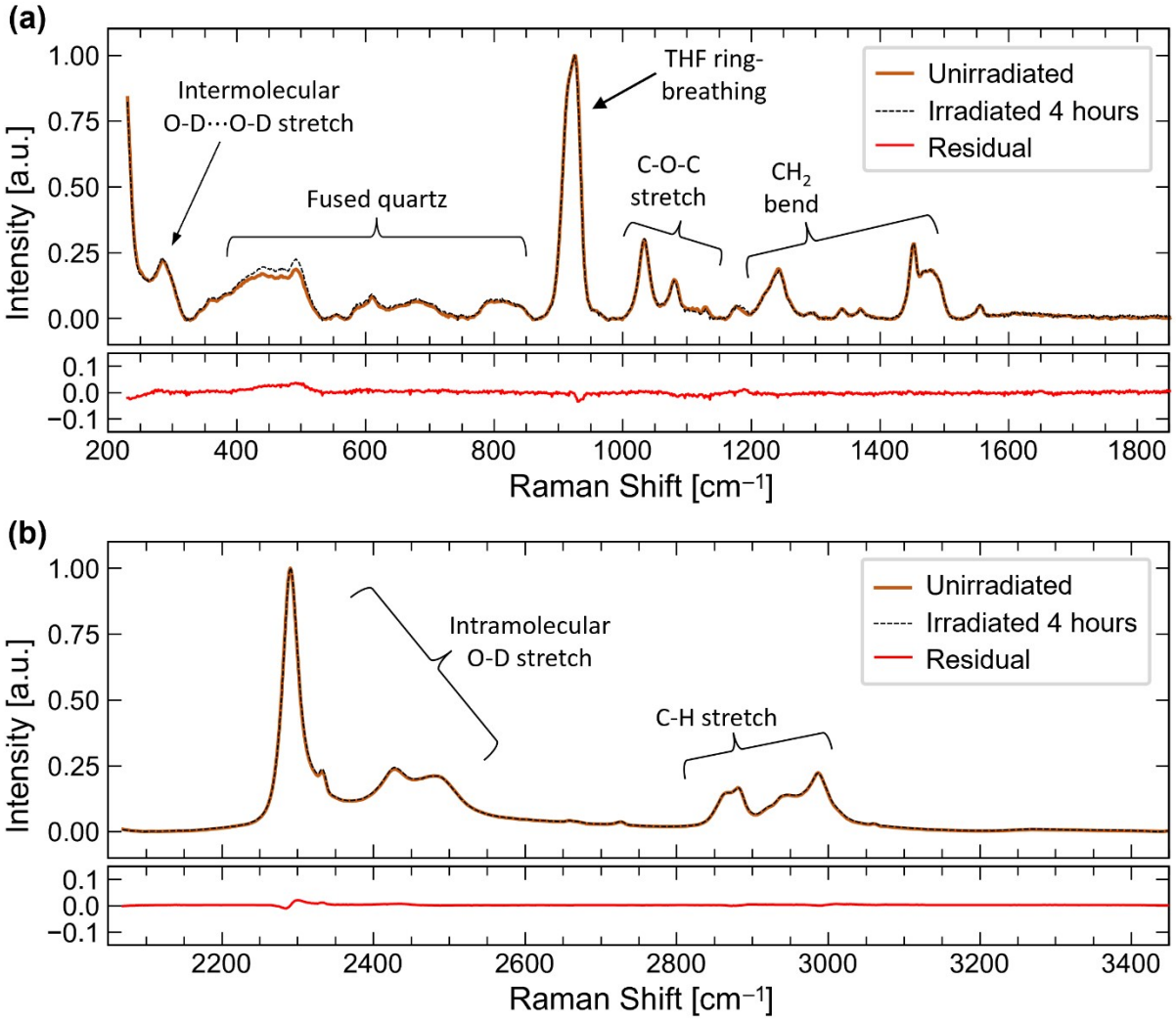

Figure S8: Normalized Raman spectra of cryogenic (77 K) D_2O/THF hydrates in the low- **(a)** and high- **(b)** frequency regions before irradiation (solid orange line), after 4 hours of irradiation (dashed black line) and the difference spectrum (solid red line). Spectra are normalized to account for changes in Raman scatter intensity due to absorption in the UV irradiated sample (see Figure S18 for unnormalized spectra). No significant structural changes or product formation occurring as a result of UV irradiation could be inferred from these spectra.

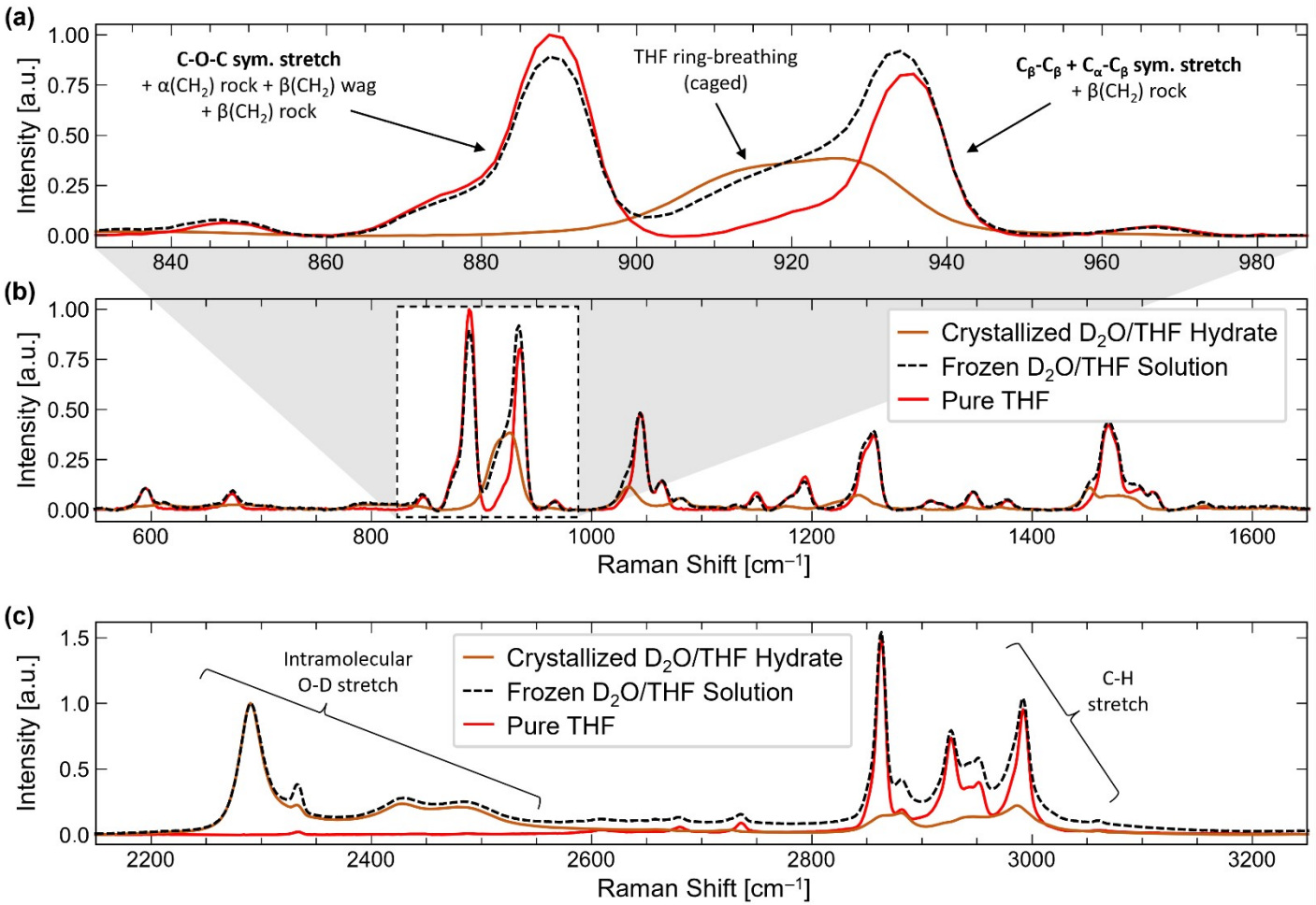

Figure S9: Raman spectra of properly crystallized D_2O/THF hydrates (solid orange line), a flash-frozen sample of the same D_2O/THF solution (dashed black line), and pure THF (solid red line), all measured at 77 K prior to irradiation. One can clearly see that the flash frozen solution simultaneously contains D_2O ice, solid THF, and THF hydrate due to improper crystallization of the latter phase. **(a)** Contains a zoom-in on the modes associated with THF ring-breathing[9,10] while **(b)** and **(c)** feature the low- and high- frequency regions respectively.

SI.3 Additional ESR Data & Analysis

SI.3a Structural Assignments for Observed Radicals

The main signal present in each of the hydrate samples (1st component in Fig. 4) arises from an unpaired electron coupling to two pairs (n = 2) of magnetically distinct nuclear spins. For the samples containing undeuterated THF, these nuclei must be protons (I = ½) to produce the observed "triple-triplet" splitting pattern of $(2nI + 1)(2nI + 1)$ = 9 lines with an intensity ratio of 1:2:2:1:4:1:2:2:1. The two pairs of protons give hyperfine coupling constants of a_α(2H) = 2.217 mT and a_β(2H) = 3.199 mT, respectively. For the sample containing d8-THF, these nuclei are deuterons (I = 1) which yield a denser, unresolved 25-line splitting pattern (Fig. S10c) with the magnitude of both hyperfine interactions reduced by a factor of g_D/g_H = 6.5144 to give a_α(2D) = 0.3375 mT and a_β(2D) = 0.4682 mT, respectively. Since isotopic labeling of THF alters the primary signal in this manner, the species giving rise to it must be derived from THF.

ESR studies of *γ*-irradiated THF hydrates report the signatures of the cyclic THF-2-yl radical, and occasionally, the less stable THF-3-yl radical, both resulting from H abstraction reactions (2) and (3), or homolytic bond cleavage at the 2- and 3-positions respectively.[11,12] However, since both these radicals exhibit a hyperfine interaction with a single magnetically distinct proton at the *α*-carbon, their spectra contain an even number of lines and can thus be ruled out as our primary photoproduct. Neither of these neutral, cyclic radicals are observed at 77 K, however, they do emerge after annealing UV irradiated hydrates above 120 K when reactions with atomic radicals are possible (Fig. S12, Table S7).

The ground-state conformer of the cyclic THF radical cation, formed via the removal of an electron from the oxygen lone-pair orbitals, has C_2 symmetry.[13] In this twisted conformation, the two pairs of hydrogens at carbons 2 and 4, respectively, are split into axial and equatorial positions, with the axial hydrogens overlapping more with the oxygen-centered spin density. While the ESR spectrum of this radical isolated in CCl_3F matrices also exhibits a 9-line splitting pattern, the magnitude of the hyperfine interactions is much too large to match, with coupling constants of a_{ax}(2H) = 8.9 mT and a_{eq}(2H) = 4.0 mT.[14] Furthermore, oxygen-centered radicals often have g-factors > 2.004 while the species observed in this study have g-factors closer to the free-electron value of 2.0023, typical of carbon centered radicals.

The ESR spectrum reported for the n-propyl radical generated in γ-irradiated propane hydrates bears a striking resemblance to the spectra of hydrates containing undeuterated THF in Figure 3, having the same intensity ratios and similar hyperfine coupling constants.[15] The spin density of this radical is centered on the terminal methylene carbon whose protons lie in the nodal plane a_α(2H) = 2.22 mT and overlaps with the protons on the adjacent carbon a_β(2H) = 2.96 mT. Given the evidence provided, we can confidently classify the dominant ESR active species isolated in the UV irradiation of THF hydrates as a 1-alkyl radical, which must be the result of ring-opening or fragmentation of the THF molecule (Table S3).[16] The precise identity of this radical cannot be concluded from these spectra alone due to the limited extent of the spin-density and its inability to probe molecular structure beyond the *α*- and β-carbon atoms.

The 1-alkyl radical sits on the shoulder of a broad singlet with a relatively low g-factor of 2.001025. In acyl radicals (O=•C–R), most of the spin-density is concentrated in a *σ*-orbital geminal to the R-group, making coupling to any protons on the R-group very limited. The resulting weak, unresolved coupling produces a broad singlet, and σ-radicals such as this typically have g-factors lower than g_e = 2.0023. As a final observation, the peak-to-peak linewidth for this feature decreases substantially in the sample containing d8-THF (0.447 mT) compared to both samples containing undeuterated THF (0.948 mT in H_2O and 0.834 mT in D_2O). This

demonstrates that the linewidth is the result of unresolved hyperfine coupling to the hydrogen nuclei of the guest, which is consistent with the description of an acyl radical (Table S4).

In the allyl radical, the delocalization of its unpaired electron spin density in π-orbitals keeps all five hydrogen nuclei in the nodal-plane. The hyperfine coupling to these nuclei is relatively weak, with the two pairs of four equivalent protons at the distal α-carbons producing a quintet with a_α(4H) = 1.484 mT splitting and the lone hydrogen at the β-carbon bifurcating these lines by an additional a_β(1H) = 0.4833 mT (Table S5).

A quartet with an intensity ratio of 1:2:2:1 from a hyperfine interaction with three equivalent hydrogen nuclei, a splitting of 2.348 mT and a g-factor of 2.002312 was also observed and could be identified as the methyl radical. This radical has a shallow, nearly planar, trigonal pyramidal geometry with spin density concentrated in a perpendicularly oriented *p* orbital (Table S6).

The high-/low-field signatures of (Fig. 3a/e) atomic hydrogen and (Fig. 3b/d) deuterium are observed in the three irradiated THF hydrate samples. The characteristic *a*(1H) = 50.1 mT doublet of $H^\bullet$ is present in all three samples while the *a*(1D) = 7.7 mT triplet of $D^\bullet$ is only seen in samples containing D_2O or d8-THF. An additional splitting of ~0.50 mT with a 1:2:1 intensity ratio can be seen in the atomic radical lines for all samples with an undeuterated host lattice. This can be simulated as a weak HFC interaction to a pair of protons of a remote water molecule. This so-called "super-hyperfine" interaction suggests that most of the observed $H^\bullet/D^\bullet$ is stabilized near the cage walls. An analogous, albeit weaker interaction is present in the organic radicals and manifests itself as an effective line-broadening in the H_2O/THF system with respect to the D_2O/THF system.

Hyperfine coupling constants *a* can be converted between units of magnetic field strength [mT] and frequency [MHz], which is used in Tables S3-7,

$$B\,[mT] = \frac{h}{g\mu_B}\nu\,[MHz] \qquad \textbf{Eqn. S3}$$

where *B* is the magnetic field strength (in units of mT) *h* is Planck's constant, *g* is the g-factor, and *v* is the corresponding resonance frequency (in units of MHz).

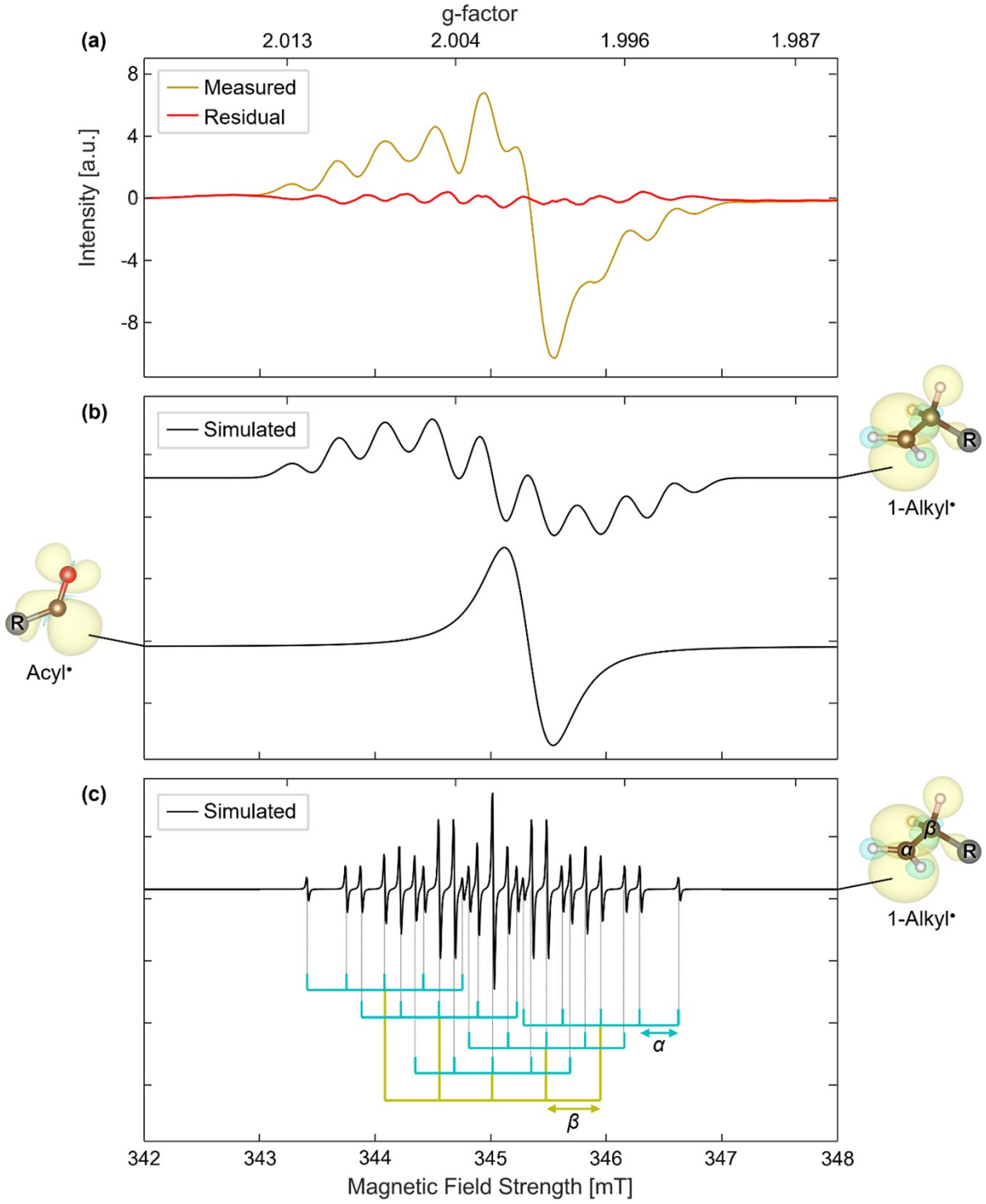

Figure S10: ESR basis analysis for irradiated H_2O/d8-THF hydrate at 77 K. **(a)** Measured spectrum (gold) and residual to the best fit (red). **(b)** Simulated component spectra of deuterated 1-alkyl, and acyl radicals. Minor species such as the deuterated methyl and allyl radicals could not be resolved at this scale. Molecular structures and spin-density plots (positive: yellow, negative: cyan) for each species are in the provided in the margins. **(c)** Simulated ESR spectrum for the deuterated 1-alkyl radical with an arbitrarily narrow

linewidth revealing the unresolved quintuple-quintet. The hyperfine coupling magnitudes for the pairs of deuterium atoms at the α- and β-carbon are indicated by cyan and yellow arrows respectively.

SI.3b Irradiated Pure Solvent Controls

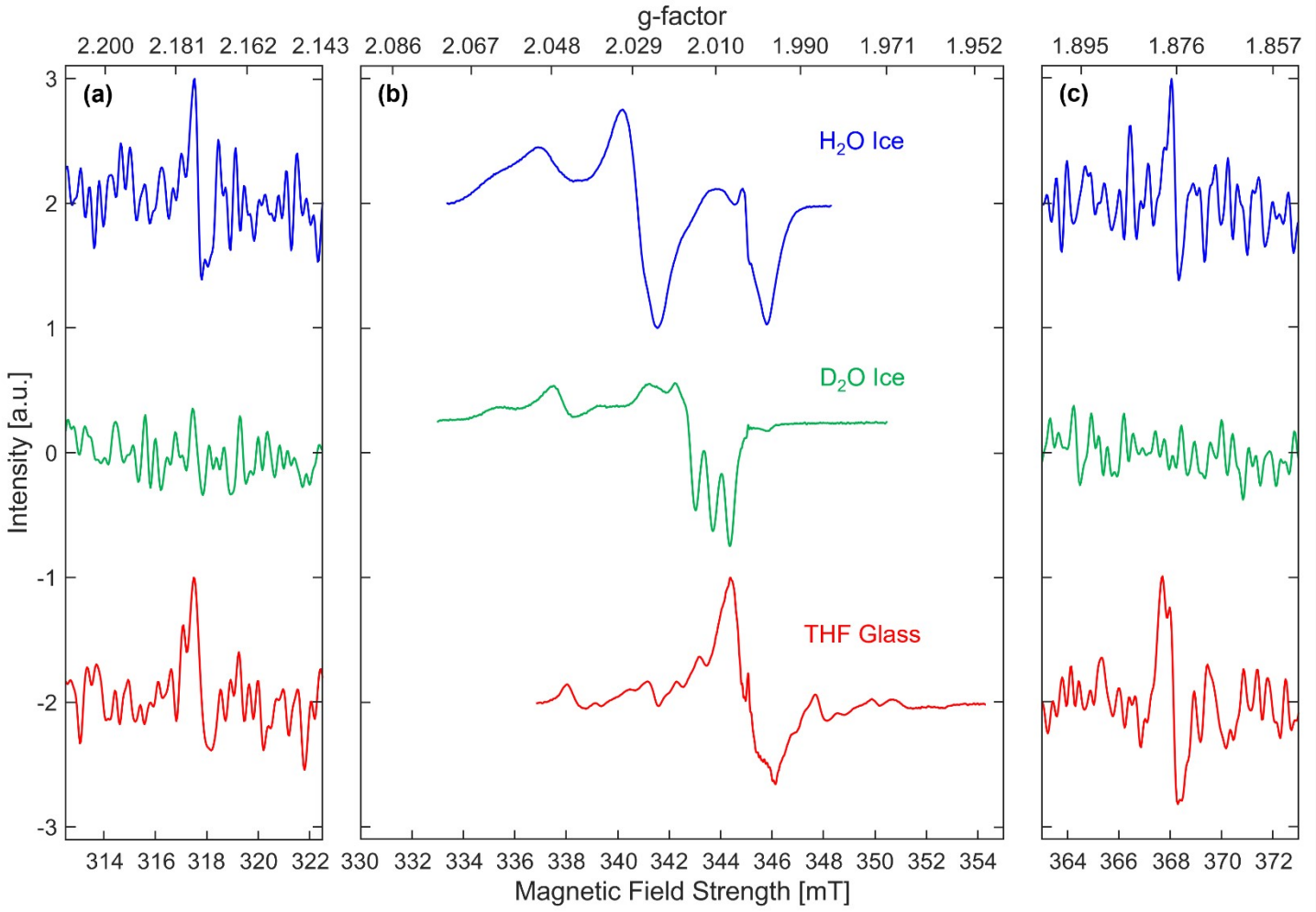

Figure S11: Normalized ESR spectra of neat components of the hydrate, (top) H_2O, (middle) D_2O, and (bottom) THF, irradiated at 77 K. **(a/c)** Weak signatures of the atomic hydrogen radical at low/high field ranges. The atomic radicals are not stabilized well in any of these pure solids compared to the hydrate. **(b)** Anisotropic signatures of (top) $OH^{\bullet}$, and (middle) $OD^{\bullet}$ stabilized in the hydrogen-bond network of amorphous ice Ih. The spectrum of glassed THF (bottom) gives a complex signal arising from carbon-centered radicals, which is difficult to interpret given the unresolvable splitting patterns.

SI.3c Temperature Dependent ESR Spectra

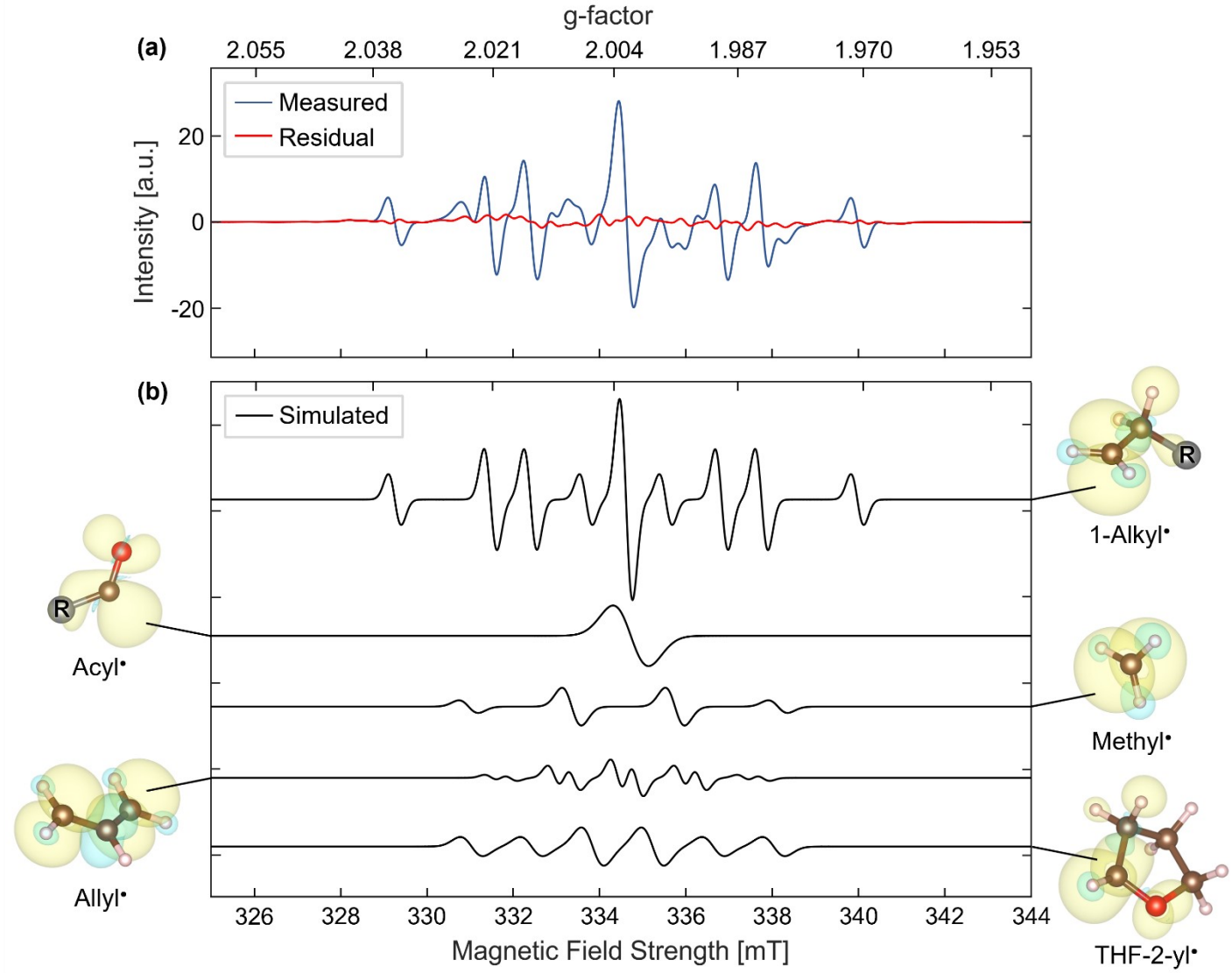

Figure S12: ESR basis analysis for irradiated H_2O/THF hydrate at 85 K after annealing > 120 K. **(a)** Measured spectrum (blue) and residual to the best fit (red). **(b)** Simulated component spectra of 1-alkyl, acyl, methyl, allyl, and THF-2-yl radicals. The appearance of the cyclic THF-2-yl radical is accompanied by the disappearance of atomic radicals after annealing above 120 K. Molecular structures and spin-density plots (positive: yellow, negative: cyan) for each species are in the provided in the margins. The measurement was performed using a Leica CM3050S Cryostat which operates at a slightly lower X-band frequency of ~9.37 GHz resulting in the bottom horizontal axis being shifted by ~10.7 mT with respect to samples measured in the liquid N_2 Dewar.

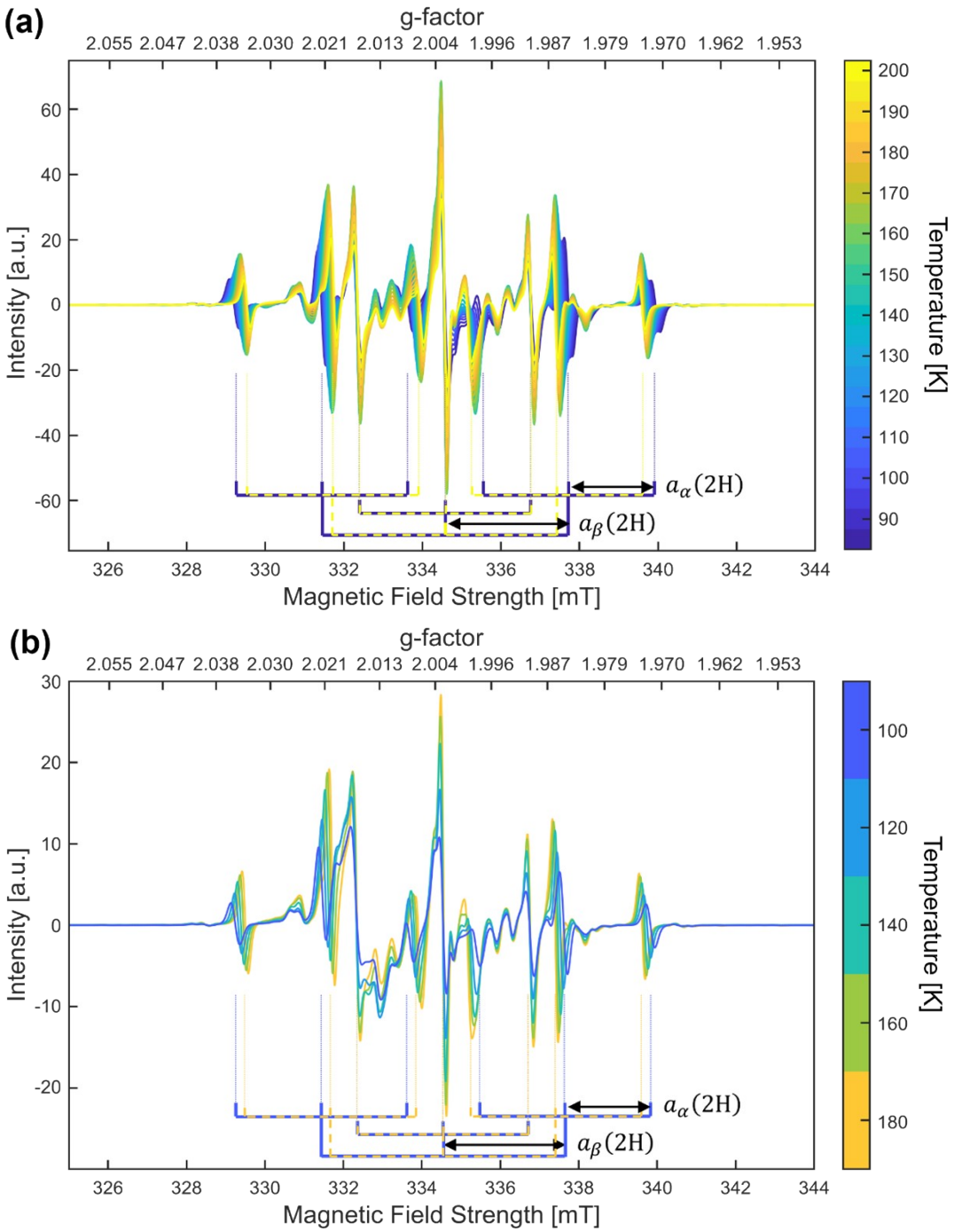

Figure S13: Temperature dependent ESR spectra of irradiated D_2O/THF hydrate following irradiation. **(a)** Warming from 85-200 K. **(b)** Cooling from 180-100 K. Line positions and hyperfine coupling magnitudes for the 1-alkyl radical are denoted with brackets and double

arrows respectively. Variations in linewidth and signal amplitude with temperature are observed. A broad singlet appears near g = 2.015 after warming to ~200 K. The radicals possess remarkable thermal stability, exhibiting only slow decay at elevated temperatures as expected from clathrate hydrates. Measurements were performed over a period of ~6 hours using a Leica CM3050S Cryostat which operates at a slightly lower X-band frequency of ~9.37 GHz resulting in the bottom horizontal axis being shifted by ~10.7 mT with respect to samples measured in the liquid nitrogen Dewar.

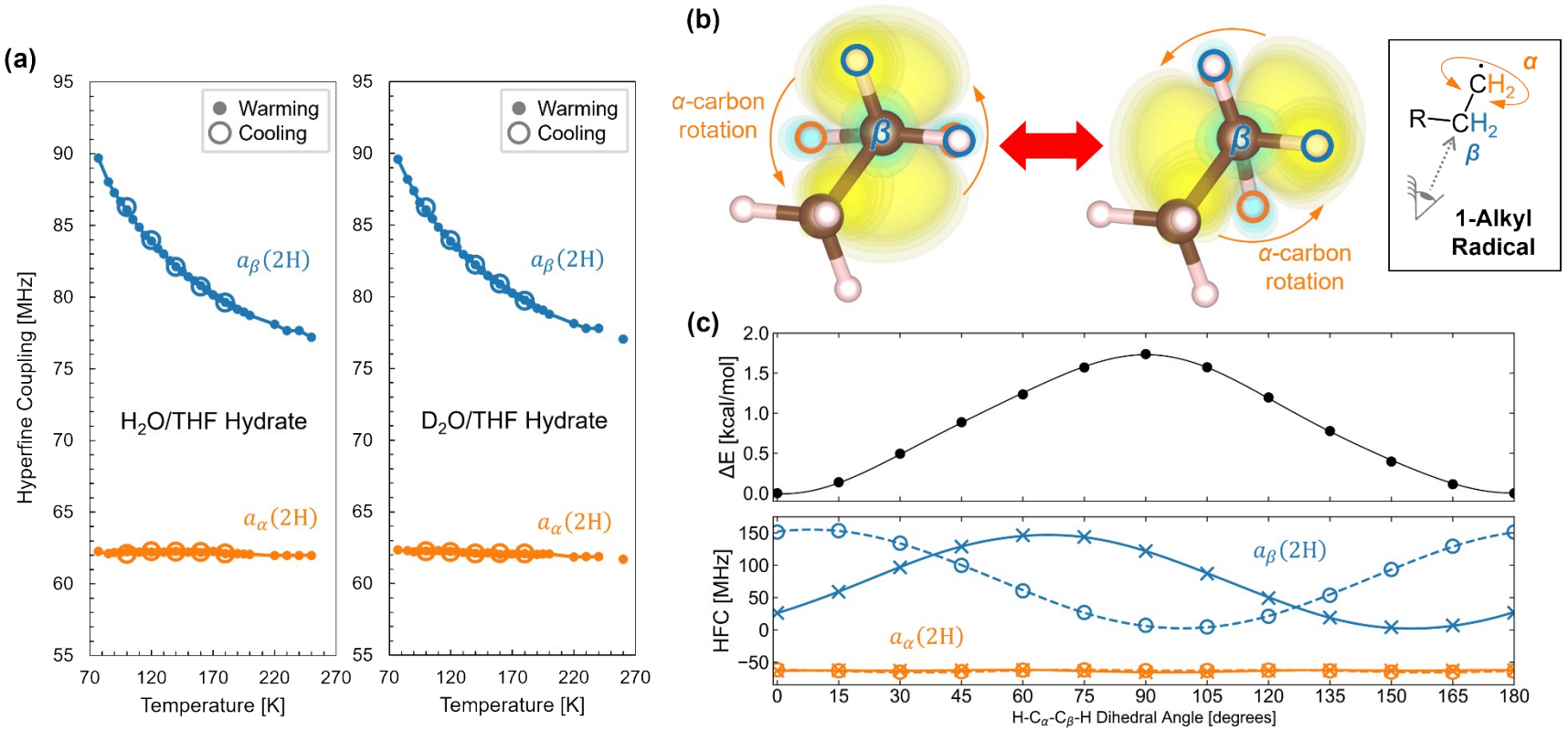

Figure S14: (a) Temperature dependence of hyperfine coupling constants for the 1-alkyl radical extracted from fits to the ESR spectra of irradiated THF hydrates. Warming and cooling cycles are plotted as closed and open circles respectively. Note how the strength of coupling to H's on the β-carbon (blue) is sensitive to temperature while the coupling to protons on the α-carbon (orange) is constant. The lack of hysteresis upon temperature cycling suggests that the changes are due to thermal motion. **(b)** Spin density plots of the n-propyl radical (1-alkyl radical) at two different H-C_α-C_β-H dihedral angles. The viewing angle is directed down the C_α-C_β bond as depicted in the top right corner. Note how the overlap of spin density localized on the α-carbon (yellow isosurfaces) with the hydrogens on the β-carbon varies with this angle. As temperature increases, the interconversion between these two conformers (red double arrow) increases leading to lower values of a thermally averaged hyperfine coupling strength. **(c)** Potential energy surface calculated using the nudged elastic band method on an image dependent pair potential surface[17] (top) and hyperfine coupling constants (bottom) for a 180° rotation about the C_α-C_β bond of an n-propyl radical within a $5^{12}6^4$ cage. The height of the rotational energy barrier was calculated to be 1.74 kcal/mol.

SI.3d Calculated & Measured ESR Parameters:

Table S3: ESR parameters for the 1-alkyl (n-propyl) radical. Calculated values (black) correspond to the "rigid-limit" given the molecular geometry (optimized within $5^{12}6^4$ hydrate cage) depicted in the spin-density plot. Hyperfine coupling (HFC) magnitudes for groups of hydrogen atoms, which are magnetically-equivalent in the high-temperature limit due to thermal motion, are averaged for a better comparison with measured values (red) extracted from simulated fits to the ESR spectrum presented in Figure 4. Values in parentheses are the equivalent values for d8-THF/H_2O or THF/D_2O hydrates.

1-Alkyl (n-propyl) radical

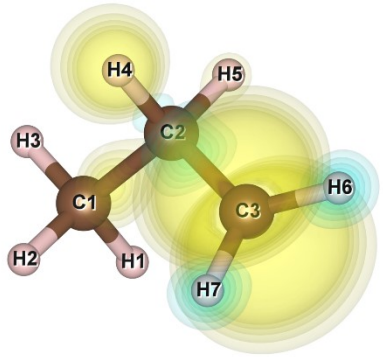

	X	Y	Z
g-eigenvalues ***Calculated***	2.002191	2.002790	2.003008
Average	2.002663		
Isotropic g-factor ***Measured***	2.002312		

	C1			C2		C3	
	H1	**H2**	**H3**	**H4**	**H5**	**H6**	**H7**
Isotropic HFC [MHz] ***Calculated***	–2.488	–1.686	3.100	151.315	26.185	–63.194	–61.714
Average (d8-THF)	–0.537 (–0.0824)			88.75 (13.62)		–62.45 (–9.587)	
Isotropic HFC [MHz] ***Measured*** **(d8-THF)**	—			89.659 (13.12)		62.129 (9.458)	
Linewidth [MHz] ***Measured*** **(D_2O, d8-THF)**	0.318179 (0.257502, 0.290833)						

Table S4: ESR parameters for the acyl (butanoyl) radical. Calculated values (black) correspond to the "rigid-limit" given the molecular geometry (optimized within $5^{12}6^4$ hydrate cage) depicted in the spin-density plot. Hyperfine coupling (HFC) magnitudes for groups of hydrogen atoms, which are magnetically-equivalent in the high-temperature limit due to thermal motion, are averaged for a better comparison with measured values (red) extracted from simulated fits to the ESR spectrum presented in Figure 4. Values in parentheses are the equivalent values for d8-THF/H_2O or THF/D_2O hydrates.

Acyl (butanoyl) radical

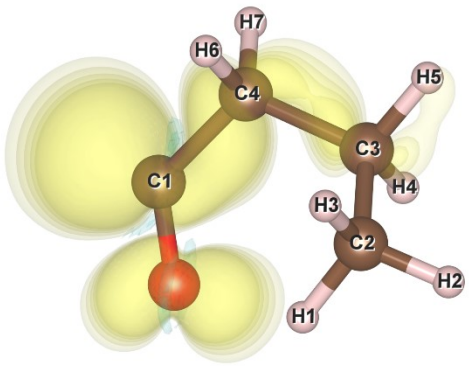

	X	Y	Z
g-eigenvalues (calculated)	1.995352	2.002014	2.004602
Average	2.000656		
Isotropic g-factor (measured)	2.001025		

	C2			C3		C4	
	H1	**H2**	**H3**	**H4**	**H5**	**H6**	**H7**
Isotropic HFC [MHz] (calculated)	2.857	3.579	–0.252	–2.773	17.906	–6.739	–9.012
Average (d8-THF)	2.061 (0.3164)			7.566 (1.161)		–7.876 (–1.209)	
Isotropic HFC [MHz] (measured)	—			—		—	
Linewidth [MHz] *Measured* (D_2O, d8-THF)	0.956236 (0.845626, 0.553939)						

Table S5: ESR parameters for the allyl radical. Calculated values (black) correspond to the "rigid-limit" given the molecular geometry (optimized within $5^{12}6^4$ hydrate cage) depicted in the spin-density plot. Hyperfine coupling (HFC) magnitudes for groups of hydrogen atoms, which are magnetically-equivalent in the high-temperature limit due to thermal motion, are averaged for a better comparison with measured values (red) extracted from simulated fits to the ESR spectrum presented in Figure 4.

Allyl radical

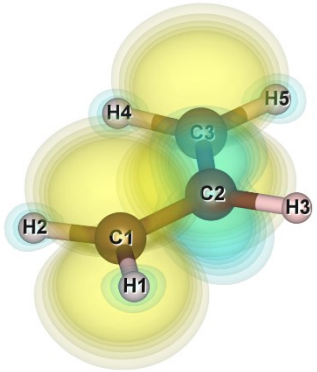

	X	Y	Z
g-eigenvalues (calculated)	2.002216	2.002839	2.002897
Average	2.002651		
Isotropic g-factor (measured)	2.002244		

	C1 & C3				C2
	H1	**H2**	**H4**	**H5**	**H3**
Isotropic HFC [MHz] (calculated)	–43.252	–40.642	–40.646	–43.136	12.305
Average	–41.919				12.305
Isotropic HFC [MHz] (measured)	41.598				13.544
Linewidth [MHz] *Measured* (D_2O)	0.287479 (0.205629)				

Table S6: ESR parameters for the methyl radical. Calculated values (black) correspond to the "rigid-limit" given the molecular geometry (optimized within $5^{12}6^4$ hydrate cage) depicted in the spin-density plot. Hyperfine coupling (HFC) magnitudes for groups of hydrogen atoms, which are magnetically-equivalent in the high-temperature limit due to thermal motion, are averaged for a better comparison with measured values (red) extracted from simulated fits to the ESR spectrum presented in Figure 4.

Methyl radical

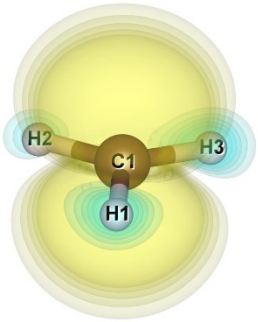

	X	Y	Z
g-eigenvalues (calculated)	2.002191	2.002790	2.003008
Average	2.002663		
Isotropic g-factor (measured)	2.002312		

	C1		
	H1	**H2**	**H3**
Isotropic HFC [MHz] (calculated)	–63.431	–63.092	–63.459
Average	–63.327		
Isotropic HFC [MHz] (measured)	65.814		
Linewidth [MHz] *Measured* (D_2O)	0.409314 (0.328119)		

Table S7: ESR parameters for the THF-2-yl radical. Calculated values (black) correspond to the "rigid-limit" given the molecular geometry (optimized within $5^{12}6^4$ hydrate cage) depicted in the spin-density plot. Hyperfine coupling (HFC) magnitudes for groups of hydrogen atoms, which are magnetically-equivalent in the high-temperature limit due to thermal motion, are averaged for a better comparison with measured values (red) extracted from simulated fits to the ESR spectrum presented in Figure S12.

Tetrahydrofuran-2-yl radical

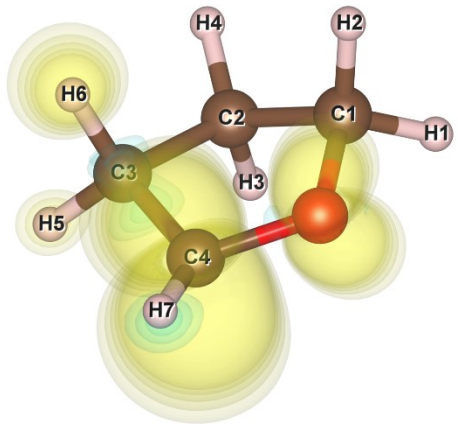

	X	Y	Z
g-eigenvalues (calculated)	2.002191	2.003564	2.004559
Average	2.003438		
Isotropic g-factor (measured)	2.003028		

	C1		C2		C3		C4
	H1	**H2**	**H3**	**H4**	**H5**	**H6**	**H7**
Isotropic HFC [MHz] (calculated)	2.451	13.793	–1.283	–1.829	41.450	117.224	–30.845
Average	8.122		1.556		79.337		–30.845
Isotropic HFC [MHz] (measured)	—		—		78.505		38.970

SI.3e Calibration to Internal Standard

Equation S4 relates an unknown number of moles N_X of species X to a known quantity N_{REF} of a reference standard through their relative signal areas A (double-integrals of 1st derivative ESR spectra), g-factors g, and spin S.

Table S8 reports radical yield estimates for a D_2O/THF hydrate irradiated at 265 nm for 2 hours. With ~2 µJ/pulse at a repetition rate of 5 kHz, approximately 10^{20} photons interacted with the sample. From these estimates based solely on the quantitation of observed ESR active species, the total quantum efficiency of 2PA is ~0.045%. The true yield may be higher if one considers any products formed though radical chain termination.

An attempt was made to detect any diamagnetic "final products" produced after thawing using H^1 NMR spectroscopy. The D_2O/THF hydrate sample utilized was irradiated for a total of 4 hours at 77 K (see Fig. S16-18), then left out at room temperature to thaw before being transferred to an NMR tube and diluted to a volume of 300 µL with D_2O. We were unable to find any discernible difference between the NMR spectrum of the thawed irradiated sample and that of an unirradiated sample taken from the same 5.88 mol% aqueous THF solution. It is possible that after recombination and dilution, the total concentration of diamagnetic products in the NMR tube might be no higher than ~250 µM which is below the instrument's detection threshold.

Radical	Yield [nmol]
1-alkyl	24.5 ± 0.3
acyl	24.0 ± 0.3
methyl	4.02 ± 0.05
allyl	2.47 ± 0.03
hydrogen	13.3 ± 0.2
deuterium	6.04 ± 0.07
Total	**74.3 ± 0.5**

Table S8: Radical product yields for the D_2O/THF hydrate irradiated at 265 nm for 2 hours by a 5 kHz train of 2 µJ pulses (~10^{20} total photons). Yield estimates were calibrated to a known quantity (N_{REF} = 34.1 ± 0.04 µmol) of $Cu(II)SO_4 \cdot 5H_2O$ using equation S4.

$$\frac{N_X}{N_{REF}} = \frac{A_X}{A_{REF}} \cdot \left[\frac{g_{REF}^2}{g_X^2} \cdot \frac{S_{REF}(S_{REF}+1)}{S_X(S_X+1)} \right] \qquad \textbf{Eqn. S4}$$

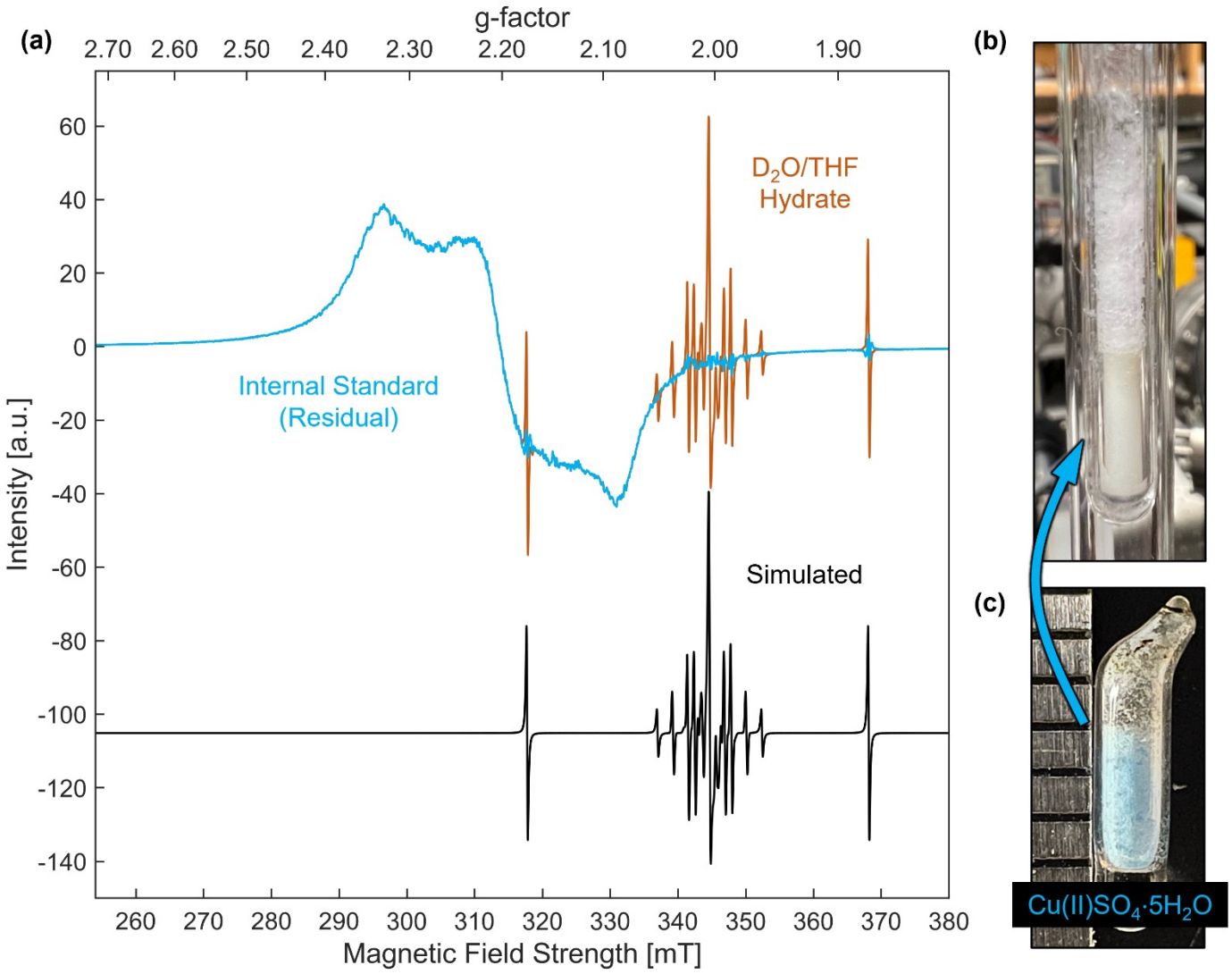

Figure S15: (a) Full-field ESR spectrum of irradiated D_2O/THF hydrate with copper(II) sulfate pentahydrate internal standard (same spectrum as Figure 3). (Orange) measured spectrum, (black) simulated fit, (cyan) residual, containing the signal from the Cu(II) internal standard. **(b)** Photograph of the ESR sample tube in the LN cold-finger Dewar. The "snow-like" THF hydrate sample is packed on top of the Cu(II) internal standard, which is contained within a cylindrical Teflon jacket. **(c)** Photograph of the Cu(II) standard inside a flame-sealed glass tube.

SI.3f Photobleaching of the ESR Singlet

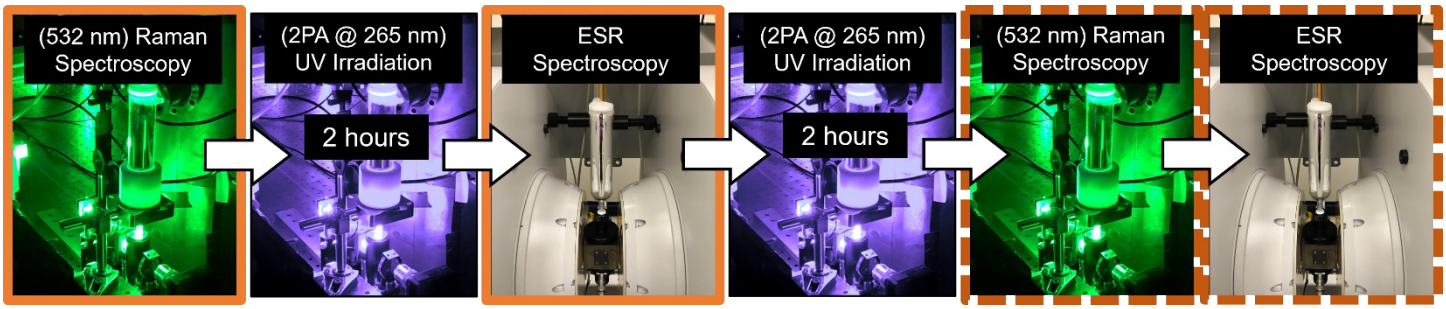

Figure S16: Experimental workflow where photobleaching of ESR singlet at *g* = 2.001 was observed. Raman and ESR spectra were measured for cryogenic (77 K) D_2O/THF hydrates before and after 2 hours of irradiation respectively (solid orange boxes). Afterwards, the same sample was irradiated for an additional 2 hours followed by an additional set of Raman and ESR measurements (dashed brown boxes). Both sets of ESR and Raman spectra are presented in Figures S17 and S18 respectively. Photobleaching of the ESR singlet produced during UV irradiation is caused by absorption of the 532 nm Raman pump laser. Images depicting UV irradiation are colorized.

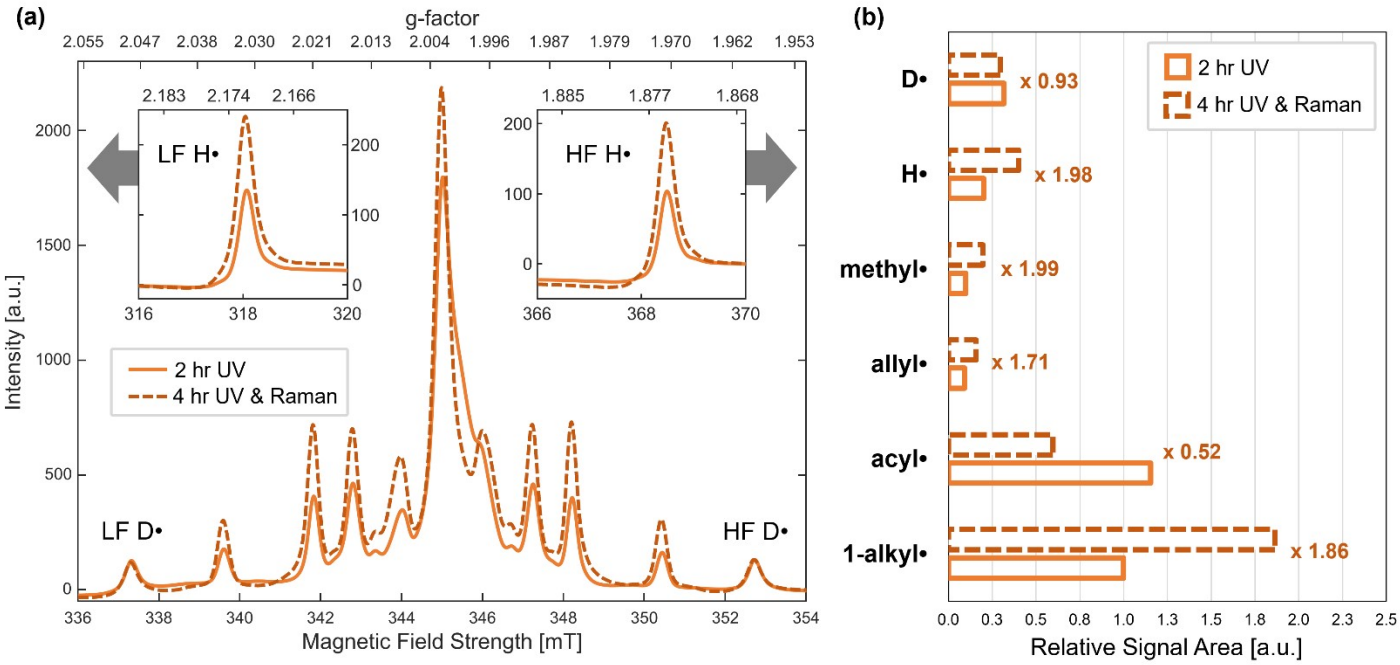

Figure S17: (a) ESR absorption spectra of cryogenic (77 K) D_2O/THF hydrates after 2 hours of UV irradiation (solid orange line) and after 4 hours of UV irradiation followed by exposure to the 532 nm Raman pump laser (dashed brown line). The insets show the low- and high-field atomic hydrogen radicals. Note the sharpening of spectral lines near *g* = 2.001 after photobleaching. **(b)** Relative signal areas for various radical species extracted from fits to the ESR spectra. Note the approximate doubling of most radicals after an additional 2 hours of UV irradiation. The area of the singlet (attributed to the acyl radical) drops due to photobleaching by the 532 nm Raman pump laser. Curiously, the amount of D• remains roughly constant between measurements while amount of H• doubles, perhaps suggestive of a kinetic isotope effect related to trapping. Since this sample was not prepared with an internal standard like the one in SI.3e, we report only relative signal areas rather than absolute yields.

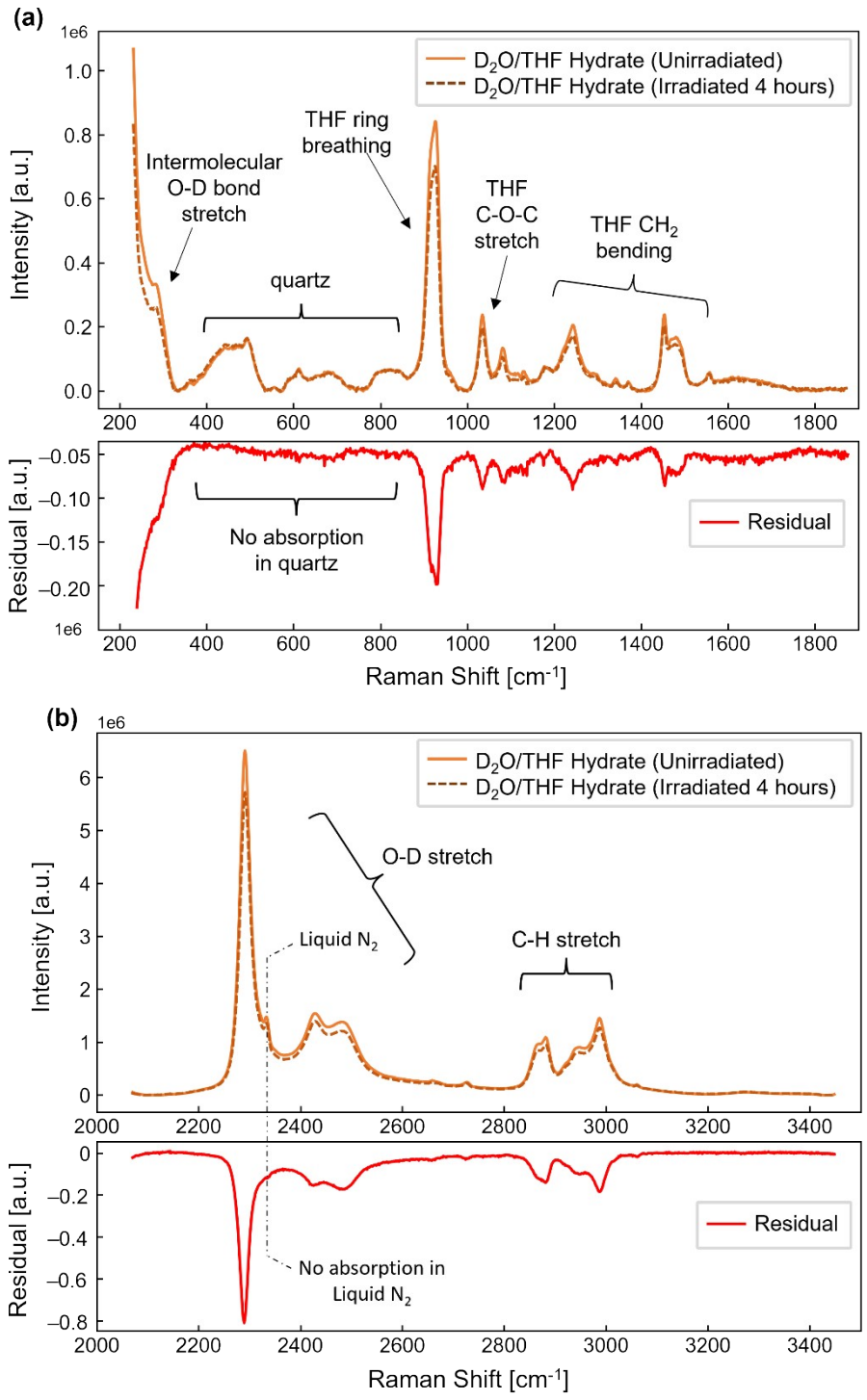

Figure S18: Unnormalized Raman spectra of cryogenic (77 K) D_2O/THF hydrates in the low- **(a)** and high- **(b)** frequency regions before irradiation (solid orange line), after 4 hours of irradiation (dashed brown line) and the difference spectrum (solid red line). A uniform drop in Raman scatter intensity for all features associated with the THF hydrate can be seen in the UV irradiated sample. This can be

attributed to absorption by acyl radicals generated during irradiation.[18–20] No such drop is observed for features associated with the quartz ESR tube, cold finger, or the liquid N_2 jacket surrounding the sample because the Raman pump encounters them first.

SI.4 Computational Methods

SI.4a Optimized Structures and Relative Energies for Proposed Photolysis Scheme

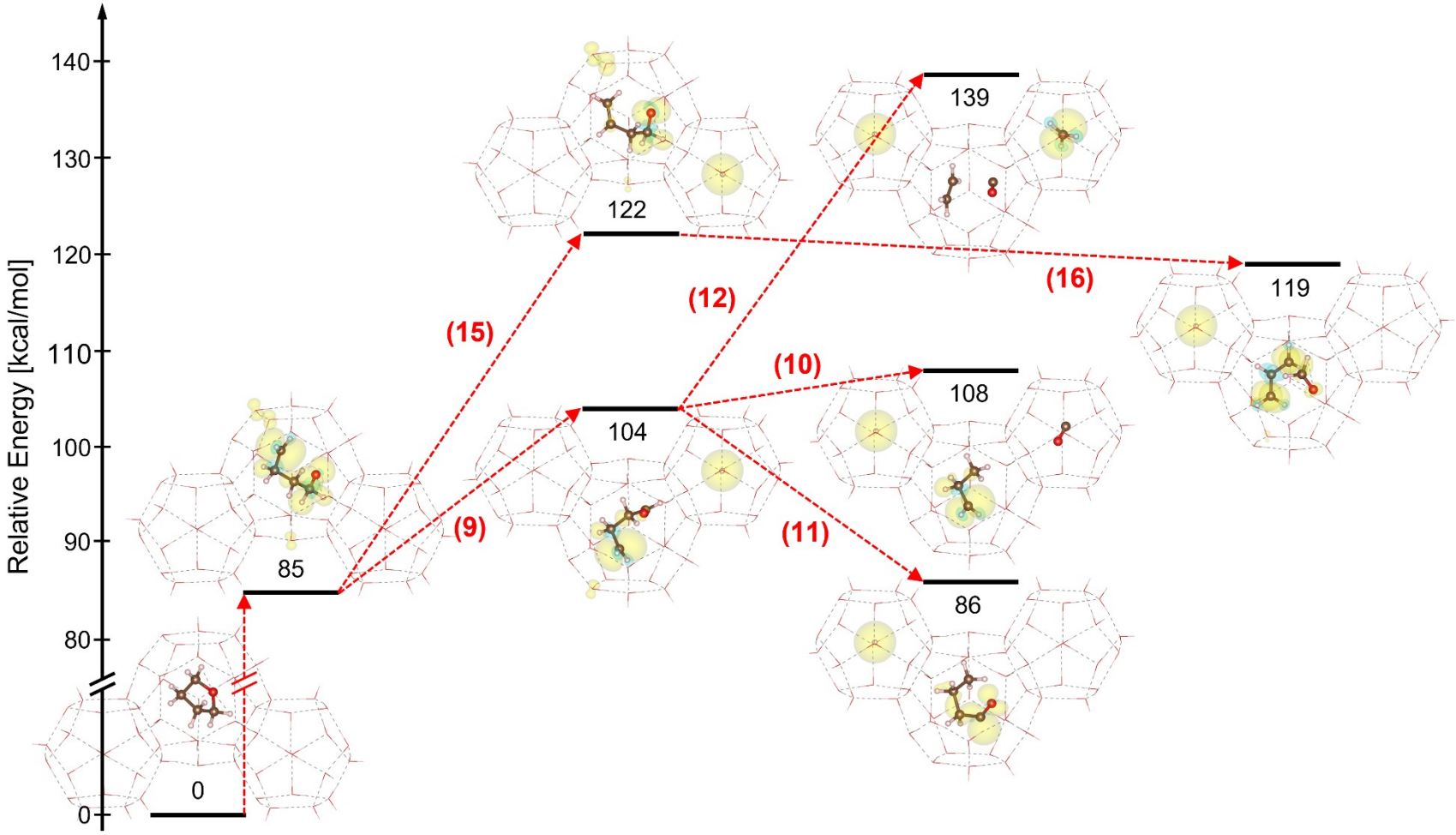

Figure S19: Computed relative energies of for the non-linear photolysis scheme proposed in Section 2.3. Optimized structures ($C_4H_{124}O_{59}$) provided for each step with spin density isosurfaces drawn (positive: yellow, negative: cyan). Transition states and activation barriers for each reaction were not calculated. The energy deposited by a pair of 265 nm photons is ~216 kcal/mol.

SI.5 — References

1 S.-J. Baek, A. Park, Y.-J. Ahn and J. Choo, *Analyst*, 2015, **140**, 250–257.
2 P. S. R. Prasad, K. Shiva Prasad and N. K. Thakur, *Spectrochimica Acta Part A: Molecular and Biomolecular Spectroscopy*, 2007, **68**, 1096–1100.
3 S. Subramanian and E. D. Sloan, *J. Phys. Chem. B*, 2002, **106**, 4348–4355.
4 L. Chen, H. Lu and J. A. Ripmeester, *Chemical Engineering Science*, 2015, **138**, 706–711.
5 M. Kato, S. Matsumoto, A. Takashima, Y. Fujii, Y. Takasu and I. Nishio, *Vibrational Spectroscopy*, 2016, **85**, 11–15.
6 C. Liu, H. Lu and Y. Ye, *Chinese Journal of Chemical Physics*, 2009, **22**, 353–358.
7 J. Qin and W. F. Kuhs, *AIChE Journal*, 2013, **59**, 2155–2167.
8 A. K. Sum, R. C. Burruss and E. D. Sloan, *J. Phys. Chem. B*, 1997, **101**, 7371–7377.
9 Y. Takasu, S. Matsumoto, Y. Fujii and I. Nishio, *Chemical Physics Letters*, 2015, **627**, 39–43.
10 B. Cadioli, E. Gallinella, C. Coulombeau, H. Jobic and G. Berthier, *J. Phys. Chem.*, 1993, **97**, 7844–7856.
11 S. Moon, S. Hong, Y. Lee, J. S. Lee, Y.-H. Ahn and Y. Park, *J. Phys. Chem. C*, 2021, **125**, 1767–1773.
12 S.-H. Yeon, J. Seol, Y. Park, D.-Y. Koh, Y. S. Kang and H. Lee, *J. Am. Chem. Soc.*, 2008, **130**, 9208–9209.
13 S. M. Park, Y. R. Lee, D. W. Kang, H. L. Kim and C. H. Kwon, *Phys. Chem. Chem. Phys.*, 2017, **19**, 30362–30369.
14 H. Kubodera, T. Shida and K. Shimokoshi, *J. Phys. Chem.*, 1981, **85**, 2583–2586.
15 T. Sugahara, Y. Kobayashi, A. Tani, T. Inoue and K. Ohgaki, *J. Phys. Chem. A*, 2012, **116**, 2405–2408.
16 A. Röder, A. B. Skov, A. E. Boguslavskiy, R. Lausten and A. Stolow, *Phys. Chem. Chem. Phys.*, 2020, **22**, 26241–26254.
17 S. Smidstrup, A. Pedersen, K. Stokbro and H. Jónsson, *J. Chem. Phys.*, 2014, **140**, 214106.
18 H. S. Judeikis and S. Siegel, *The Journal of Chemical Physics*, 2004, **43**, 3625–3638.
19 A. G. Davies, R. Sutcliffe, L. Wc and H. Oaj, 1980, 6.
20 S. Noda, K. Fueki and Z. Kuri, *The Journal of Chemical Physics*, 1968, **49**, 3287–3292.